PCCP

ROYAL SOCIETY OF CHEMISTRY

PAPER

View Article Online
View Journal



Cite this: DOI: 10.1039/d5cp01917f

# Alkali diffusion in niobium doped $SrTiO_3$ – transport pathways, diffusion coefficients and activation energies†

Janek Bernzen and Karl-Michael Weitzel *

The diffusion characteristics of potassium and rubidium in niobium-doped strontium titanate single crystals were systematically investigated over a range of temperatures. Charge attachment induced transport (CAIT) experiments were employed to induce diffusion by continuous deposition of alkali ions onto the sample surface. Subsequent analysis of the samples using time-of-flight secondary ion mass spectrometry (ToF-SIMS) depth profiling revealed bimodal concentration profiles for all experiments, for both potassium and rubidium. These profiles were modeled assuming a superposition of two mechanisms, identifying two distinct transport pathways, each characterized by a specific diffusion coefficient. The temperature dependence of the diffusion coefficients was evaluated using an Arrhenius approach, enabling the determination of two activation energies for each alkali ion. The process with a lower diffusion coefficient and lower activation energy is attributed to interstitial transport, while the process with a higher diffusion coefficient and higher activation energy correlates with diffusion mediated by defects and is similar between the alkali ions. This study provides insight into the complex interplay between defect chemistry and ion transport mechanisms in niobium-doped strontium titanate, following a previous study on potassium diffusion in undoped strontium titanate.

Received 21st May 2025,
Accepted 13th July 2025

DOI: 10.1039/d5cp01917f

rsc.li/pccp



## 1. Introduction

Perovskite oxide materials, particularly those containing transition metals, are widely recognized for their versatility and outstanding properties, making them ideal for various electrochemical and electronic applications. Their role in key technologies, such as hydrogen production through water electrolysis,[1,2] solid oxide fuel cells (SOFCs),[3–6] resistive random-access memory (RRAM),[7,8] high-temperature superconductors[9] and many more,[10,11] highlights their potential to contribute significantly to a wide range of applications, including the decarbonization of our economy. Among these materials, the ability of perovskites to accommodate significant doping levels and incorporate a wide variety of elements enables the fine-tuning of their properties for specific applications.[12–14]

Strontium titanate ($SrTiO_3$, STO) serves as a model system for perovskite oxides due to its well-defined cubic crystal structure, high crystalline stability, robust resistance to atmospheric corrosion and flexibility for chemical modifications. While the ionic mobility of oxygen vacancies in $SrTiO_3$ is well-documented, cationic transport remains comparatively less explored, particularly for dopants and non-native ions.[15,16] This knowledge gap is significant, as the ability of perovskites to incorporate foreign ions is fundamental to their versatility in material properties. For example, the electrical conductivity of STO films can be changed by three orders of magnitude by doping with specific amounts of niobium.[17]

In a previous study, we demonstrated that the diffusion of potassium in strontium titanate single crystals gives rise to well-defined concentration depth profiles, from which diffusion coefficients and activation energies for the relevant diffusion mechanisms could be derived. That analysis revealed the coexistence of two diffusion processes – one involving interstitial sites and the other vacancy mediated.[18]

Building on this prior work, the present study focuses on the diffusion dynamics of potassium and rubidium in niobium-doped strontium titanate, with the aim of deepening our understanding of alkali mobility in this material system. It is well-established that the lattice parameter of perovskite oxides, particularly strontium titanate, is influenced by doping,[19–21] and this dependency generally extends to activation energies for ionic transport as well.[22,23] Consequently, variations in diffusive behavior are anticipated, driven by the interplay between dopant-induced structural modifications and the resulting changes in the energy landscape.

*Department of chemistry, Philipps-Universität, Marburg, Germany.*
*E-mail: weitzel@chemie.uni-marburg.de*

† Electronic supplementary information (ESI) available. See DOI: https://doi.org/10.1039/d5cp01917f

The diffusion profiles were generated in charge attachment induced transport (CAIT) experiments, which is conceptually a unidirectional ion exchange experiment. Detailed descriptions of the CAIT technique can be found in previous publications.[24–29] In the experiments, an alkali ion beam (in this case $K^+$ or $Rb^+$) was directed onto niobium-doped and monocrystalline strontium titanate samples. By varying the sample temperature, temperature-dependent diffusion profiles were formed and subsequently characterized using time-of-flight secondary ion mass spectrometry (ToF-SIMS) depth profiling. The temperature dependence of the diffusion profiles enabled the determination of activation energies associated with the underlying diffusion mechanisms.

# 2. Materials and methods

## 2.1. Sample preparation

Single crystals of niobium-doped strontium titanate (Nb:STO, 0.5 mass-% Nb corresponding to $x$ = 0.01 in notation $SrTi_{1-x}Nb_xO_3$), synthesized using the Verneuil method, with crystal growth oriented approximately along the [100] direction, were used for the experiments. According to the manufacturer (CrysTec GmbH Kristalltechnologie, Berlin, Germany), the sample surface was oriented along the [100] crystallographic plane and had an epipolished finish on one side. The crystals have the dimensions of 10 mm × 5 mm × 1 mm. For experimental purposes, the samples were fixed to a copper sample holder using a silver-based, electronically conductive adhesive, ensuring robust electrical and thermal contact.

## 2.2. Charge attachment induced transport

The charge attachment induced transport (CAIT) technique is a sophisticated experimental method for probing charge carrier mobility in solid electrolytes. A comprehensive description of the method is provided in the literature.[24,25,28] The CAIT approach enabled both the determination of sample conductivities and the generation of ionic transport profiles. This was achieved by depositing charge carriers onto the sample surface *via* a low-energy ion beam. Specifically, beams of $K^+$ and $Rb^+$ ions were employed, generated through thermionic emission from aluminosilicate emitters. These ions, with a kinetic energy of 10 eV, were guided to the sample using an electrostatic lens system. The emitters consisted of $KAlSi_2O_6$ and $RbAlSi_2O_6$, each combined with molybdenum powder in a mass ratio of 1 : 9 to ensure stable charge balancing. These materials were heated to approximately 1100 K, and an extraction field of −2 kV was applied to facilitate ion emission. Further details on the synthesis and properties of these thermionic emitters are available in the literature.[30] To monitor the ion beam intensity during the experiment, a 95%-transmission molybdenum mesh was positioned in front of the sample to measure the neutralization current. A stainless-steel mask with a circular aperture (diameter: 4 mm) was used to confine the ion attachment area. The charge flow through the sample to the grounded backside electrode was measured using an in-house developed transimpedance amplifier ammeter. Temperature regulation was achieved using a Eurotherm 3216 temperature controller equipped with a Pt100 thermometer, coupled with a custom-built resistance heating system. The entire experiment was conducted under high vacuum conditions ($10^{-5}$ mbar) to prevent oxidation of the emitter and ensure a collision-free path for the ions. After the experiment, the sample was rapidly cooled to room temperature to minimize further ionic movements. For additional information on the CAIT technique and experimental setup, readers are referred to the literature.[24,25,28]

## 2.3. ToF-SIMS depth profiling

In this study, a time-of-flight secondary ion mass spectrometer (ToF-SIMS 4, IONTOF, Münster, Germany) was employed to characterize the concentration–depth profiles generated during the CAIT experiments. Secondary ions were extracted from the sample surface using a liquid metal ion gun (LMIG) that delivered a pulsed beam of high-energy bismuth ions ($E_{kin}$ = 25 keV). These secondary ions were subsequently analyzed in a reflectron ToF-MS, operating in bunched mode to achieve a mass resolution of up to $m/\Delta m$ = 10 000. To mitigate surface charging effects, a 20 eV electron flood beam was directed at the sample during the analysis. The surface was scanned across an area of 100 μm × 100 μm, yielding a two-dimensional mass spectrum with a resolution of 128 × 128 data points. Depth resolution was achieved by incremental removal of the sample surface using a 2 keV $O_2^+$ sputter gun, which created a sputter crater with lateral dimensions of 300 μm × 300 μm. The ToF-SIMS measurements produced a three-dimensional data set containing $>10^7$ mass spectra. The concentration–depth profiles presented in this work were derived from the raw data by summing the intensities of the selected ion fragments across the lateral dimensions of the crater and applying a Poisson correction.[31] The resulting intensity profiles are, to a good approximation, proportional to the ion concentrations at specific sputter depths. Following the ToF-SIMS analysis, the total depth of the sputter crater was determined using a tactile profilometer (Bruker DekTak XT, Billerica, USA). This step enabled the conversion of sputtering time into an absolute depth scale, ensuring precise spatial characterization of ion distributions.

# 3. Results

The diffusive behavior of the alkali ions, potassium and rubidium, in niobium-doped single-crystalline strontium titanate was studied, with a particular focus on their dependence on variations in the sample temperature $T_S$. Utilizing the charge attachment induced transport (CAIT) technique with ion beams of potassium and rubidium, diffusion profiles of these ions were generated within the material over time. These profiles were subsequently analyzed and characterized through ToF-SIMS depth profiling. Throughout the CAIT experiments, the sample temperatures were maintained at 160 °C, 180 °C and 200 °C, respectively, ensuring stable and controlled experimental conditions – enabling a reliable

investigation of the thermal influence on ionic diffusion within the material.

### 3.1. Data normalization

The diffusion profiles presented in this study were obtained using time-of-flight secondary ion mass spectrometry (ToF-SIMS). This technique excels in visualizing spatially resolved concentration profiles and offers a comparatively high signal-to-noise ratio for alkali cations such as $K^+$ and $Rb^+$. With a depth resolution of up to 1 nm (as specified by the manufacturer), ToF-SIMS provides highly accurate representations of diffusion profiles, even for shallow penetration depths and low concentrations. However, it should be noted that ToF-SIMS raw data do not directly yield absolute concentration or depth information. Instead, the raw output represents secondary ion intensities as a function of sputtering time. To interpret these data as concentration–depth profiles, appropriate normalization is required.

Depth information is derived from the sputtering time $t_S$, which corresponds to the duration for which the $O_2^+$ sputter gun has bombarded the sample surface during the ToF-SIMS experiment and is proportional to the resulting crater depth. The actual depth is determined by multiplying the sputtering time $t_S$ with the sputtering rate $r_S = \Delta x/\Delta t$, defined as the depth increment $\Delta x$ per unit time $\Delta t$. The sputtering rate depends on several parameters, including the intensity and energy of the sputtering beam as well as the material properties of the sample. To accurately establish the sputtering rate, post-analysis is performed using a tactile profilometer (DekTak XT). By measuring the crater depth and dividing it by the total sputtering time, a constant sputtering rate is assumed, which is justified by the monophasic nature of the sample.

The secondary ion intensity represents the number of ions of a specific species detected using a ToF-SIMS system within a single slice of data (128 × 128 primary ion pulses). Poisson correction is applied to these intensity values to compensate for detector saturation artifacts caused by the dead time of the microchannel plates (MCPs).[31] All intensity profiles presented in this work have been Poisson corrected. It is well established that Poisson-corrected ToF-SIMS intensities are proportional to the concentration of the corresponding fragment.[32] However, converting these proportional values into absolute concentrations is non-trivial, as the proportionality factor depends on various factors, such as the primary ion beam intensity and the chemical environment of the fragment being ionized. Consequently, normalization must be tailored to the specific data set.

In many CAIT studies, stoichiometric replacement of native ions with foreign ions has been used to normalize transport profiles of the latter.[33–35] This approach assumes a macroscopic displacement mechanism for native ions, which is not applicable to the data in this study. As a result, deriving explicit concentration values would be speculative due to the lack of reliable normalization criteria. Instead, the analysis focuses on the determination of diffusion coefficients, which are independent of the absolute scaling of the diffusion profiles. To avoid conveying inaccurate concentration values, the ToF-SIMS intensity data were directly employed to represent the profiles and calculate diffusion coefficients.

In summary, the intensity profiles presented here should be interpreted as being proportional to the ion concentration, without implying explicit concentration values.

### 3.2. Diffusion profiles

The diffusion of potassium and rubidium ions in niobium-doped strontium titanate during CAIT experiments is modeled assuming adherence to Fick's second law (1).

$$\frac{\partial c(x,t)}{\partial t} = D \cdot \frac{\partial^2 c(x,t)}{\partial x^2} \tag{1}$$

Under the boundary conditions specific to CAIT, particularly the continuous ion attachment at the sample surface, an analytical solution to the diffusion equation is derived. This solution takes the form of a conjugate Gaussian error function, representing the spatial and temporal distributions of the ions within the material (2).[36]

$$c(x,t) = c_0 \cdot \mathrm{erfc}\left(\frac{x}{\sqrt{4Dt}}\right) \tag{2}$$

In this context, $x$ represents the distance from the sample surface. For a given diffusion time $t$ and surface concentration $c_0$, the diffusion profile is only dependent on the diffusion coefficient $D$. As a result, the diffusion coefficient can be extracted from the profile and utilized as a regression parameter describing the observed transport dynamics.

However, the measured diffusion profiles exhibit a pronounced bimodal characteristic, particularly evident when visualized on a logarithmic scale. Such bimodal transport behavior, indicative of competing diffusion pathways, has previously been demonstrated in the context of potassium diffusion in single crystals of undoped strontium titanate.[18] The use of a linear combination of two conjugate Gaussian error functions (3) has proven to be an effective model for describing the obtained depth profiles in that context and is equally applicable to the data presented in this study.

$$c(x,t) = c_{0,1} \cdot \mathrm{erfc}\left(\frac{x}{\sqrt{4D_1 t}}\right) + c_{0,2} \cdot \mathrm{erfc}\left(\frac{x}{\sqrt{4D_2 t}}\right) \tag{3}$$

When performing regression analysis by minimizing the sum of squared errors, the superposition of two processes with significantly different intensities often results in a bias toward the dominant process. This can lead to the suppression of the less intense process, as slight measurement inaccuracies and noise affect its representation. To reduce this effect, the regression criterion was adjusted to minimize the sum of squared errors in logarithmic space. This approach effectively reduces the influence of intensity differences, which are then represented as an offset, allowing for a more balanced characterization of both processes. The regression criterion used for the analysis is given by eqn (4).

$$\min_{c_{0,1},c_{0,2},D_1,D_2} \sum_{i=1}^{n} [\ln(y_i) - \ln(c(x_i,t))]^2 \tag{4}$$

Based on this approach, the regression model provides an excellent fit to the experimental data and four regression

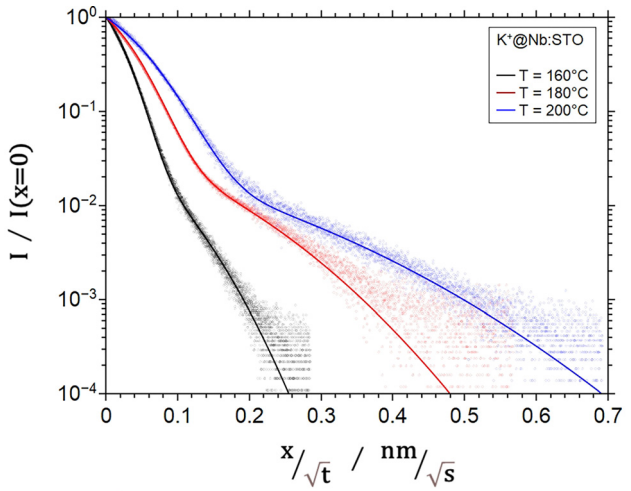


Fig. 1 ToF-SIMS concentration profiles for potassium in single crystals of Nb-doped STO overlayed with the proposed model.

parameters as output – $c_{0,1}$, $c_{0,2}$, $D_1$ and $D_2$. Fig. 1 and 2 show the obtained diffusion profiles, overlayed with the proposed model. The individual concentration depth profiles are provided in Fig. S2 and S3 of the ESI† (additional experimental parameters and regression parameters are provided in Table S1 of the ESI†). In the following, particular focus will be placed on the two diffusion coefficients, $D_1$ and $D_2$, as they serve as key metrics for comparing the different experiments conducted in this study.

As expected, the diffusion coefficients increase with increasing sample temperature. For rubidium, the diffusion coefficients at equivalent sample temperatures are consistently lower than those for potassium, which is plausible when considering the difference in ionic radii.

The ionic mobility of alkali ions in niobium-doped strontium titanate can be described as thermally activated due to the potential landscape of crystalline solids consisting of a large number of local minima and maxima. The mobile ions are preferably located in the minima – so called sites and need to pass an activation barrier in order to change their position. The height of this barrier is termed activation energy $E_A$. In thermal equilibrium, the thermal energy of the ions in the sample can be assumed to be Boltzmann distributed. Based on this, the temperature dependence of the diffusion coefficient can be described using the Arrhenius eqn (5).

$$D = D_0 \cdot \exp\left(-\frac{E_A}{k_B T}\right) \quad (5)$$

In reverse, for a given set of diffusion coefficients at different temperatures, an activation energy can be derived using a linear regression approach ($E_A = -k_B \, \partial \ln(D)/\partial T^{-1}$). Each activation energy is specific to a particular diffusion mechanism and reflects the unique energy barrier associated with that process. Given that the obtained diffusion profiles suggest the superposition of two distinct diffusion mechanisms, it is reasonable to assume the presence of two different activation energies. These activation energies can be determined from the diffusion coefficient data presented above, providing further insight into the individual transport processes contributing to the observed ionic mobility. The Arrhenius curves derived from the measured diffusion coefficients are shown in Fig. 3.

The activation energies obtained for rubidium are higher than those for potassium, which is not surprising given the larger ionic radius of rubidium. The smaller of the two diffusion coefficients is comparatively low and exhibits a high degree of similarity across the alkali ions studied.

### 3.3. Electrical conductivity

Prior to the diffusion experiments, the electrical conductivity of the samples was also investigated in DC conductivity measurements. A decrease in electrical conductivity with increasing temperature was observed (*cf.* Fig. S1 of the ESI†), qualitatively consistent with the findings reported in the literature.[20] This behavior is the characteristic of metallic conductors.

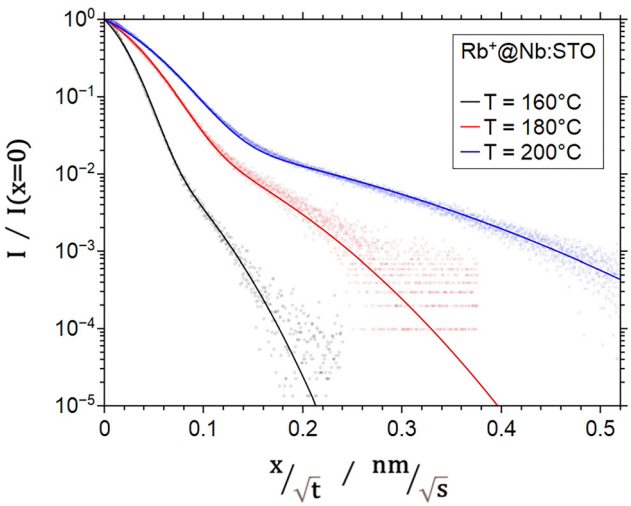


Fig. 2 ToF-SIMS concentration profiles for rubidium in single crystals of Nb-doped STO overlayed with the proposed model.

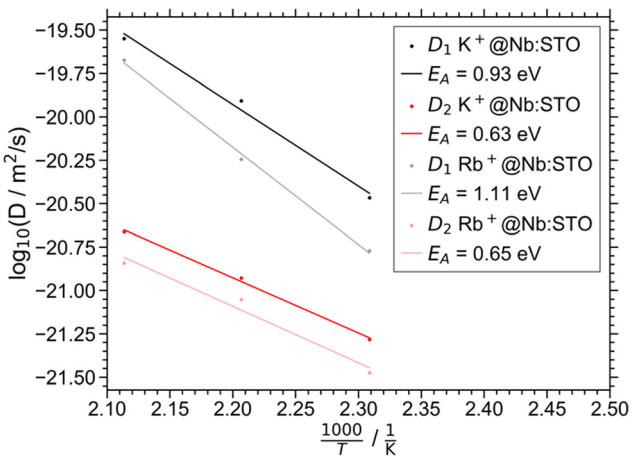


Fig. 3 Arrhenius plot of diffusion coefficients derived from experiments on Nb-doped STO single crystal samples. Potassium diffusion coefficients are shown in darker shades and rubidium diffusion coefficients are shown in lighter shades.

Due to the metallic conductivity properties of niobium-doped strontium titanate, surface charging of the sample is negligible in this case. There is an indication of alkali metal deposition at the front side probably originating from recombination of alkali ions with electrons (see Fig. S2 and S3 of the ESI†). From the current measured during the CAIT experiment integrated over time, we estimate an upper limit for the concentration of the alkali ions in the region near to the surface of Nb:STO of 5 at%. Evidently, the formation of an electric field across the sample does not occur and all transport can be interpreted as diffusion. This observation justifies the application of Fick's second law as the basis for the regression model described earlier.

The Arrhenius plot in the following Fig. 3 shows a linear regression of the data points for both observed processes.

## 4. Discussion

In the course of this study, bimodal diffusion profiles were observed for all six diffusion experiments presented. All profiles were successfully described using the proposed regression model, allowing for the extraction of twelve diffusion coefficients. The temperature dependence of these coefficients follows the Arrhenius equation, as expected, underscoring that the obtained regression parameters correspond to actual diffusion coefficients. From the Arrhenius analysis, activation energies for the underlying diffusion mechanisms were determined.

The CAIT method, while effective in providing diffusion profiles, does not reveal the atomic-level mechanisms underlying the observed processes. However, the determination of activation energies and the identification of two overlapping diffusion processes offer valuable insights and a basis for discussing potential mechanisms. The accurate description of the profiles using a linear combination of two conjugate Gaussian error functions implies that the diffusion mechanisms are, at least approximately, independent. Given that the samples are single crystals, eliminating grain boundaries and dislocation pipes as likely pathways, the observed mechanisms are most plausibly attributed to point defects and interstitial transport.

To interpret the results obtained in this study, a direct comparison with a previous investigation of potassium transport in undoped strontium titanate single crystals is particularly insightful.[18] Therefore, in CAIT experiments conducted under comparable conditions, a similar temperature series of diffusion profiles were examined. Two activation energies, 1.23 eV and 1.74 eV, were identified. These diffusion experiments were complemented by STEM analysis and DFT+$U$ calculations. Based on the comprehensive findings, the mechanism associated with the lower activation energy was assigned to the interstitial transport of potassium ions, as it showed strong agreement with the simulation results. The second mechanism, characterized by the higher activation energy, was assigned to vacancy-mediated diffusion, likely dominated by strontium vacancies.

When going from the $K^+$@STO experiment of Bernzen *et al.*[18] to the $K^+$@Nb:STO and $Rb^+$@Nb:STO experiment in this work, the two diffusion coefficients and the two activation energies change. However, there is one very clear analogy between the three data sets. In all cases, the slow process carries an amplitude about a factor of 50 larger than that of the faster process. Indeed, the slower process would not be observable, if it had lower intensity. Here, the fact is that the shape of all concentration depth profiles is the same, implying that a corresponding intensity ratio of the two transport processes is considered to strongly support that the assignment of transport mechanisms should be the same. As a consequence, we suggest to assign the slower process with lower activation energy (but higher amplitude) to interstitial transport (red traces in Fig. 3) and the faster process with higher activation energy to defect mediated transport. A direct overlay of the Arrhenius curves for potassium diffusion in doped and undoped strontium titanate is found in the ESI† in Fig. S4.

Based on this assignment, it would be justified to conclude that in going from the STO to the Nb:STO all activation energies decrease but the diffusion coefficients increase.

The decrease in activation energies may arise from several factors. Firstly, as shown in this study, niobium-doped strontium titanate shows metallic conductivity. The electronic structure of metallic conductors is significantly better equipped to compensate for local charge imbalances compared to semiconductors, such as undoped strontium titanate.

Secondly, niobium ($Nb^{5+}$) has a larger ionic radius than titanium ($Ti^{4+}$). It is well established that such dopants can expand the crystal lattice,[19–21] a factor known to reduce activation energies for diffusion.[22,23] On the other hand, for Nb doping of 0.5 wt%, the lattice expansion is probably smaller than 0.05% or 0.001 Å, making this a minor effect.[20] Thirdly, in strontium titanate, niobium functions as a donor dopant, increasing the electron density within the crystal lattice. This enhanced electron density, although delocalized over the crystal lattice, may exert an attractive force on cations, facilitating their diffusion through reduced energy barriers.

For potassium diffusion in undoped STO, the defect mediated pathways were concluded to involve strontium vacancies.[18] Given the similarity of transport characteristics observed, it seems at least likely that the potassium and rubidium transport here also correlate with strontium vacancies. Alternatively, one could consider the involvement of oxygen vacancy transport, which has been extensively discussed for undoped STO.[37–39] A typical activation energy discussed for oxygen vacancy diffusion in undoped STO is one of 0.6 eV. We note that this number is similar to the lower values reported in Table 2. On the other hand, the introduction of Nb doping increases the concentration of Sr vacancies. The fact that the diffusion coefficients observed in the Nb:STO are larger than those in the STO also supports the assignment of the fast process to Sr vacancy-mediated transport. From another point, given the negative redox potential of the alkali ions offered to the Nb:STO, it does not seem very likely that this particle favors oxygen vacancies with an effectively positive partial charge.

Table 1 Diffusion coefficients $D_1$ and $D_2$ measured for samples indicated

| Sample | $T$ [K] | $D_1$ [cm$^2$ s$^{-1}$] | $D_2$ [cm$^2$ s$^{-1}$] |
|---|---|---|---|
| $K^+$@Nb:STO 1 | 433.15 | $3.42 \times 10^{-17}$ | $5.22 \times 10^{-18}$ |
| $K^+$@Nb:STO 2 | 453.15 | $1.24 \times 10^{-16}$ | $1.18 \times 10^{-17}$ |
| $K^+$@Nb:STO 3 | 473.15 | $2.82 \times 10^{-16}$ | $2.18 \times 10^{-17}$ |
| $Rb^+$@Nb:STO 1 | 433.15 | $1.70 \times 10^{-17}$ | $3.35 \times 10^{-18}$ |
| $Rb^+$@Nb:STO 2 | 453.15 | $5.70 \times 10^{-17}$ | $8.89 \times 10^{-18}$ |
| $Rb^+$@Nb:STO 3 | 473.15 | $2.12 \times 10^{-16}$ | $1.44 \times 10^{-17}$ |

Table 2 Activation energies $E_A$ and pre-exponential factors derived from the measured diffusion coefficients

| $E_{A,1}$/eV | | $D_{0,1}$/cm$^2$ s$^{-1}$ | $E_{A,2}$/eV | $D_{0,2}$/cm$^2$ s$^{-1}$ |
|---|---|---|---|---|
| $K^+$@Nb:STO | 0.93 | $2.7 \times 10^{-6}$ | 0.63 | $1.2 \times 10^{-10}$ |
| $Rb^+$@Nb:STO | 1.11 | $1.4 \times 10^{-4}$ | 0.65 | $1.2 \times 10^{-10}$ |

As listed in Table 1, the pre-exponential factor for the Arrhenius expression is on the order of $10^{-10}$ cm$^2$ s$^{-1}$ for the pathway assigned to interstitial transport but on the order of $10^{-6}$ cm$^2$ s$^{-1}$ or even $10^{-4}$ cm$^2$ s$^{-1}$ for the transport concluded to be vacancy-mediated for $K^+$ and $Rb^+$, respectively. This may be considered surprising since this trend is opposite to the trend in intensity contribution. For the time being, the physical interpretation of the pre-exponential factors is difficult. As a consequence, we suggest to perform a systematic study of diffusion coefficients and their activation energy and pre-factors as a function of the Nb doping concentration and possibly also as a function of the Sr vacancy concentration in the future.

Future work will certainly benefit from involving high level theory and/or XPES identification of oxidation states. The analysis of the diffusion coefficients and activation energies presented does not depend on the assumption of a specific oxidation state of the alkali element.

## 5. Summary

In this study, two independent transport pathways were identified for both potassium and rubidium diffusion in niobium-doped strontium titanate. Through systematic variation of the sample temperature, two activation energies for each alkali ion were extracted from the diffusion profiles, corresponding to the distinct diffusion mechanisms. Based on a comparison with a previous publication on potassium diffusion in undoped strontium titanate, the diffusion mechanism associated with the smaller activation energy and at the same time the smaller $D$ and the higher intensity was attributed to interstitial diffusion. The process with the larger activation energy and at the same time the larger $D$ and the smaller amplitude was assigned to defect transport.

## Conflicts of interest

There are no conflicts to declare.

## Data availability

The data described in this work will be made available upon request.

## Acknowledgements

This research project is funded by the German Science Foundation (DFG) as part of the research unit FOR 5065 (“Energy Landscapes and Structure in Ion Conducting Solids”, ELSICS) project number 428906592 (project P1).

## References

1 S. Tasleem and M. Tahir, *Renewable Sustainable Energy Rev.*, 2020, **132**, 110073.
2 S. Tasleem and M. Tahir, *Int. J. Hydrogen Energy*, 2020, **45**, 19078.
3 Y. L. Lee, J. Kleis, J. Rossmeisl and D. Morgan, *Phys. Rev. B:Condens. Matter Mater. Phys.*, 2009, **80**, 224101.
4 Y. L. Lee, J. Kleis, J. Rossmeisl, S. H. Yang and D. Morgan, *Energy Environ. Sci.*, 2011, **4**, 3966.
5 I. C. Man, H. Y. Su, F. Calle-Vallejo, H. A. Hansen, J. I. Martínez, N. G. Inoglu, J. Kitchin, T. F. Jaramillo, J. K. Nørskov and J. Rossmeisl, *ChemCatChem*, 2011, **3**, 1159.
6 J. Suntivich, H. A. Gasteiger, N. Yabuuchi, H. Nakanishi, J. B. Goodenough and Y. Shao-Horn, *Nat. Chem.*, 2011, **3**, 546.
7 T. M. Shaw, S. Trolier-McKinstry and P. C. McIntyre, *Annu. Rev. Mater. Sci.*, 2000, **30**, 263.
8 M. Mrovec, J. M. Albina, B. Meyer and C. Elsässer, *Phys. Rev. B:Condens. Matter Mater. Phys.*, 2009, **79**, 245121.
9 D. W. Murphy, S. Sunshine, R. B. van Dover, R. J. Cava, B. Batlogg, S. M. Zahurak and L. F. Schneemeyer, *Phys. Rev. Lett.*, 1987, **58**, 1888.
10 A. K. Jena, A. Kulkarni and T. Miyasaka, *Chem. Rev.*, 2019, **119**, 3036.
11 Y.-H. Kim, S. Kim, A. Kakekhani, J. Park, J. Park, Y.-H. Lee, H. Xu, S. Nagane, R. B. Wexler, D.-H. Kim, S. H. Jo, L. Martínez-Sarti, P. Tan, A. Sadhanala, G.-S. Park, Y.-W. Kim, B. Hu, H. J. Bolink, S. Yoo, R. H. Friend, A. M. Rappe and T.-W. Lee, *Nat. Photonics*, 2021, **15**, 148.
12 R. Roy, *J. Am. Ceram. Soc.*, 1954, **37**, 581.
13 H. Chen, C. Lim, M. Zhou, Z. He, X. Sun, X. Li, Y. Ye, T. Tan, H. Zhang, C. Yang, J. W. Han and Y. Chen, *Adv. Sci.*, 2021, **8**, 2102713.
14 Y. Liu, C. Ye, S.-N. Zhao, Y. Wu, C. Liu, J. Huang, L. Xue, J. Sun, W. Zhang, X. Wang, P. Xiong and J. Zhu, *Nano Energy*, 2022, **99**, 107344.
15 S. Koerfer, R. A. de Souza, H.-I. Yoo and M. Martin, *Solid State Sci.*, 2008, **10**, 725.
16 J. Martin, M. Gräf, T. Kramer, C. Jooss, M.-J. Choe, K. Thornton and K.-M. Weitzel, *Phys. Chem. Chem. Phys.*, 2017, **19**, 9762.
17 T. Tomio, H. Miki, H. Tabata, T. Kawai and S. Kawai, *J. Appl. Phys.*, 1994, **76**, 5886.
18 J. Bernzen, C. Fuchs, T. Jacob, Q. Ma, T. Meyer, C. Jooss and K.-M. Weitzel, *Adv. Mater. Interfaces*, 2024, **11**, 2400338.

19 A. Janotti, B. Jalan, S. Stemmer and C. G. van de Walle, *Appl. Phys. Lett.*, 2012, **100**, 262104.
20 P. Blennow, A. Hagen, K. Hansen, L. Wallenberg and M. Mogensen, *Solid State Ionics*, 2008, **179**, 2047.
21 T. Ishihara, H. Matsuda and Y. Takita, *J. Am. Chem. Soc.*, 1994, **116**, 3801.
22 U. Kiessling, J. Claus, G. Borchardt, S. Weber and S. Scherrer, *J. Am. Ceram. Soc.*, 1994, **77**, 2188.
23 A. Yamaji, *J. Am. Ceram. Soc.*, 1975, **58**, 152.
24 M. Schäfer and K.-M. Weitzel, *Phys. Chem. Chem. Phys.*, 2011, **13**, 20112.
25 P. V. Menezes, J. Martin, M. Schafer and K.-M. Weitzel, 2011 – 14th International Symposium on Electrets, IEEE 2011, p. 37.
26 K.-M. Weitzel, L. Rossrucker, P. V. Menezes, J. Zakel, M. Schäfer and B. Roling, *Z. Phys. Chem.*, 2012, **226**, 341.
27 V. Wesp, M. Hermann, M. Schäfer, J. Hühn, W. J. Parak and K.-M. Weitzel, *Phys. Chem. Chem. Phys.*, 2016, **18**, 4345.
28 K. M. Weitzel, *Diffus. Found.*, 2016, **6**, 107.
29 S. Schulze, M. Schäfer, A. Greiner and K.-M. Weitzel, *Phys. Chem. Chem. Phys.*, 2013, **15**, 1481.
30 T. Kolling, A. Schlemmer, C. Pietzonka, B. Harbrecht and K.-M. Weitzel, *J. Appl. Phys.*, 2010, 107.
31 T. Stephan, J. Zehnpfenning and A. Benninghoven, *J. Vac. Sci. Technol., A*, 1994, **12**, 405.
32 *ToF-SIMS: Surface Analysis by Mass Spectrometry*, ed. J. C. Vickerman, D. Briggs, IM Publications and SurfaceSpectra Limited, Nottingham, 2001.
33 J. Martin, S. Mehrwald, M. Schäfer, T. Kramer, C. Jooss and K.-M. Weitzel, *Electrochim. Acta*, 2016, **191**, 616.
34 A. Hein, M. Schäfer and K.-M. Weitzel, *Solid State Ionics*, 2019, **339**, 114997.
35 K. Rein, Leitfähigkeits und Elektropolingstudien an ionenleitenden Alkali-Aluminium-Germanium-Phosphat-Gläsern, Marburg 2020.
36 N. Perez, *Electrochemistry and Corrosion Science*, Springer, Cham, 2016.
37 A. E. Paladino, L. G. Rubin and J. S. Waugh, *J. Phys. Chem. Solids*, 1965, **26**, 391.
38 I. Denk, F. Noll and J. Maier, *J. Am. Ceram. Soc.*, 1997, **80**, 279.
39 R. A. de Souza, *Adv. Funct. Mater.*, 2015, **25**, 6326.